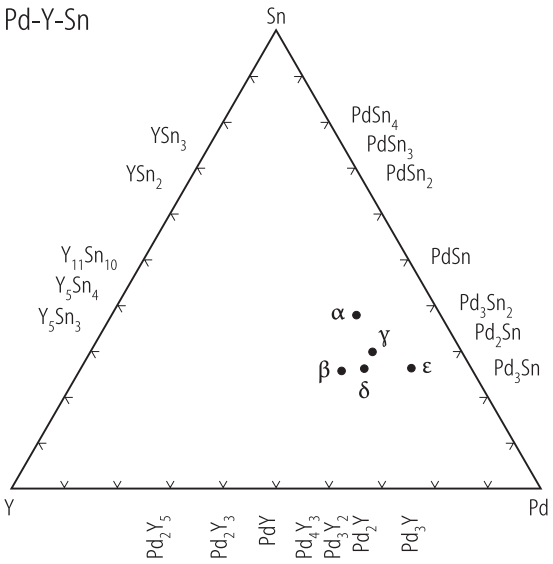

Fig. 36. Ternary phase diagram of the Pd–Y–Sn system. Of the new ternary compounds α, β, γ, δ and ε reported only the structure of the α and β phases could be determined. The α phase forms peritectically at 1228 K with a hexagonal structure with space group P6/mmm and lattice parameters a = 19.891 Å. Pd_2YSn, the β phase forms congruently at 1748 K, with the Heusler $L2_1$ structure [85J3].

Fig. 38. Microprobe analysis in the two- and three-phase regions in Pd–Y–Sn [85J3].

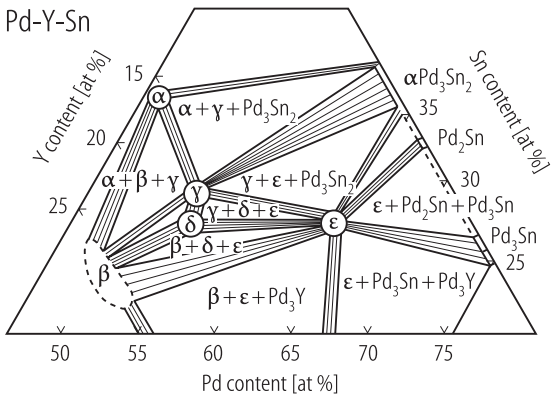

Fig. 37. Isothermal section of the partial Pd–Y–Sn system at 1075 K. The tie lines for the two-phase fields are schematic [85J3].

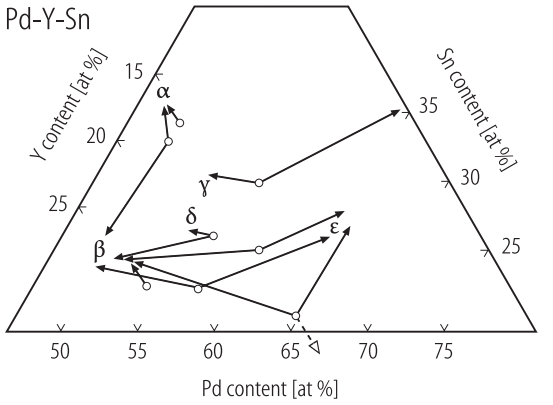

1.5.5.2.3 Kinematics of phase transition

The kinematics of the atomic ordering process were reviewed previously [88W1]. Further work has appeared on the Cu–Mn–Al system. As indicated in Table 10, the phase diagram is particularly complicated. Of particular interest is the simultaneous occurrence of two types of structural phase transition: the order-disorder transformations in the range of β phase and the decomposition of the β phase in the temperature range of its metastability.

The stability of metastable precipitates with the $L2_1$ structure has been investigated in Fe–Nb–Al up to 600 °C as a function of time.

The precipitation reaction has been studied in the Ni–Ti–Al system with the aim of improving the creep behaviour. Upon cooling, the alloys undergo a spinodal-ordering reaction.

Disorder trapping has been investigated in a rapid cooled Ni_2TiAl specimen. The alloy formed from the melt with the non-equilibrium B2 structure transforms to the $L2_1$ structure on cooling to room temperature.

Table 10. Values of the parameters of the Johnson-Mehl-Avrami type functions, the sum of which was fitted to the experimentally obtained time dependence of electrical resistivity of the alloy Cu_2MnAl at temperatures T. Here R_∞ denotes the sum of R'_∞ and R''_∞ [85S2]. Cf. Fig. 39.

T [K]	R'_0 [10^{-6} Ω]	R''_0 [10^{-6} Ω]	R_∞ [10^{-6} Ω]	τ' [min]	τ'' [min]	N'	N''
663	2	7435	15 250	147	4172	1	1.71
690	25	7207	15 717	462	3186	1	1.78
716	1066	6405	15 160	2244	753	1	1.72
740	1301	3960	14 680	265	150	1	1.86
757	1600	3653	10 423	174	68	1	1.89
773	1489	3357	13 755	110	54	1	2.13
798	1063	2741	15 044	53	36	1	1.76
813	1065	4207	12 206	27	23	1	1.98
843	1970	3744	15 064	24	17	1	3.38
873	1042	2994	19 126	10	8	1	5.48

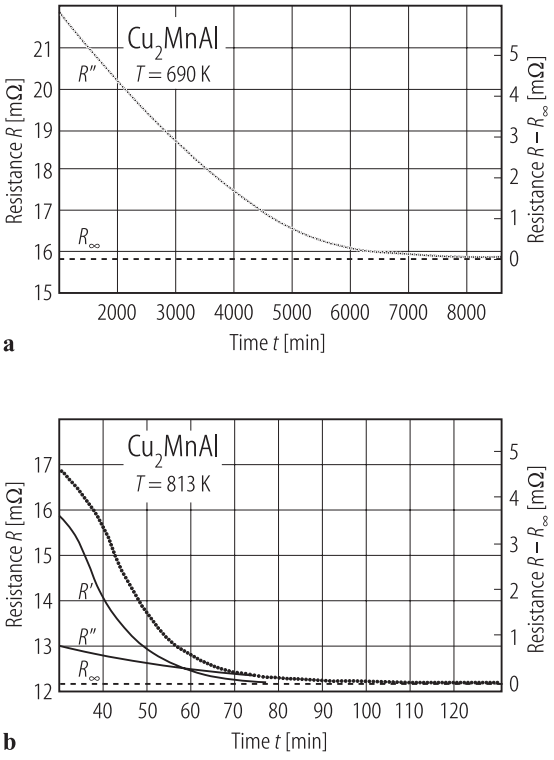

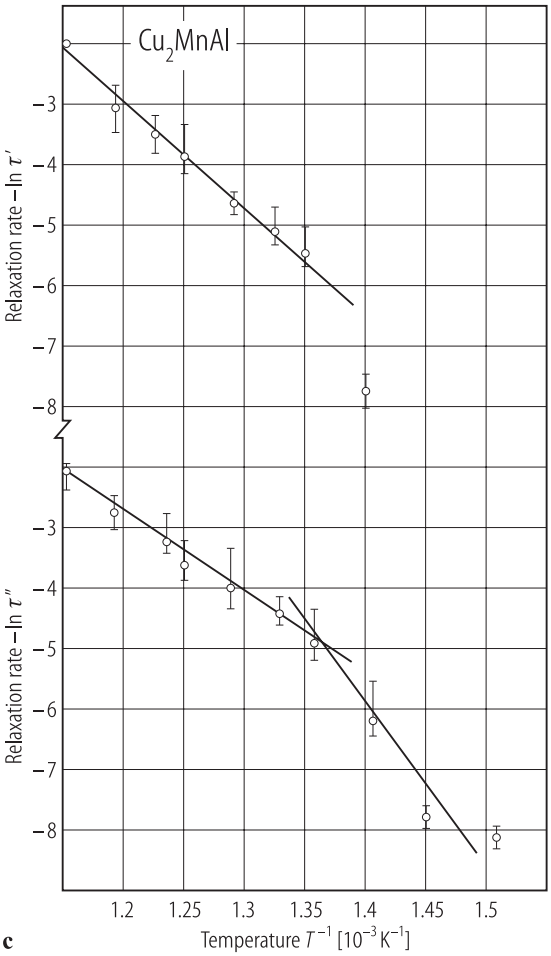

Fig. 39. Isothermal measurement of the time dependence of the electrical resistance of Cu_2MnAl. The sum of two Johnson-Mehl-Avrami type functions $R' = R_\infty + R'_0 \exp\left(-\left(\frac{t - t_V}{\tau'}\right)N\right)$ was fitted to the data. The results of this fit are given in Table 10. (**a**) T = 690 K and (**b**) T = 813 K; (**c**) shows the temperature dependence of the relaxation times τ' and τ'', both in min [85S2].

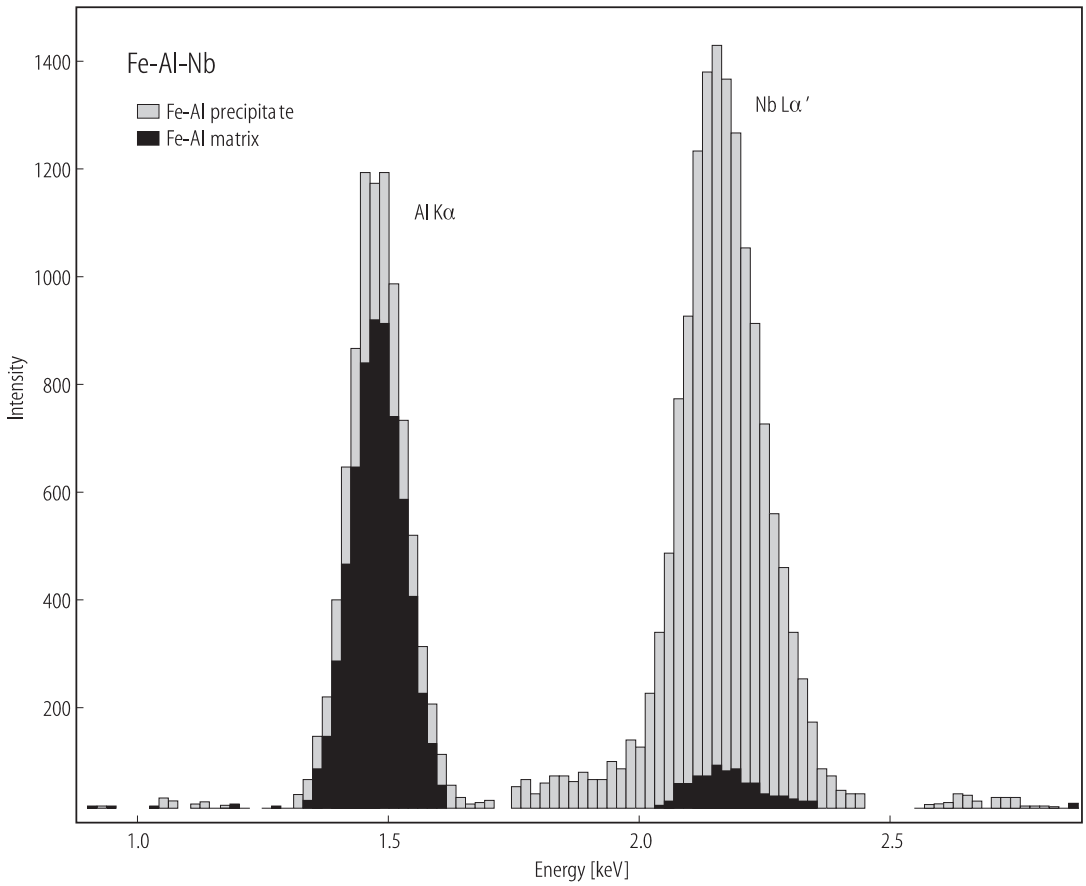

Fig. 40. Superimposed EDS spectra and analysed compositions from the precipitate and matrix phases of Fe–Al–Nb [88D2].

Composition - atomic percentage

Element	Matrix	Precipitate
Fe	75.3	61.2
Al	23.3	24.9
Nb	1.4	13.9

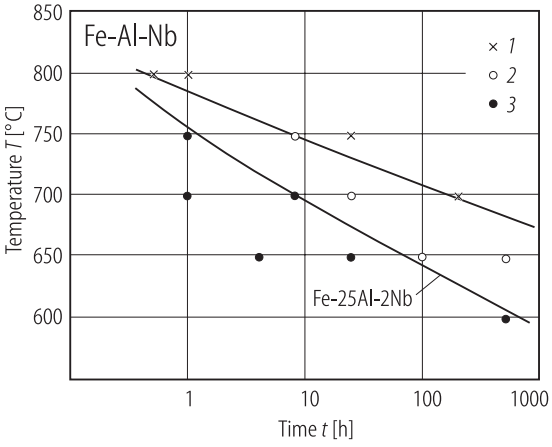

Fig. 41. Time-temperature transformation curves for the precipitation of the Heusler phase and the equilibrium C14 phase in Fe–Al–Nb *1*: stable C14 phase, *2*: two phase $L2_1$ + C14, *3*: metastable $L2_1$ only [88D2].

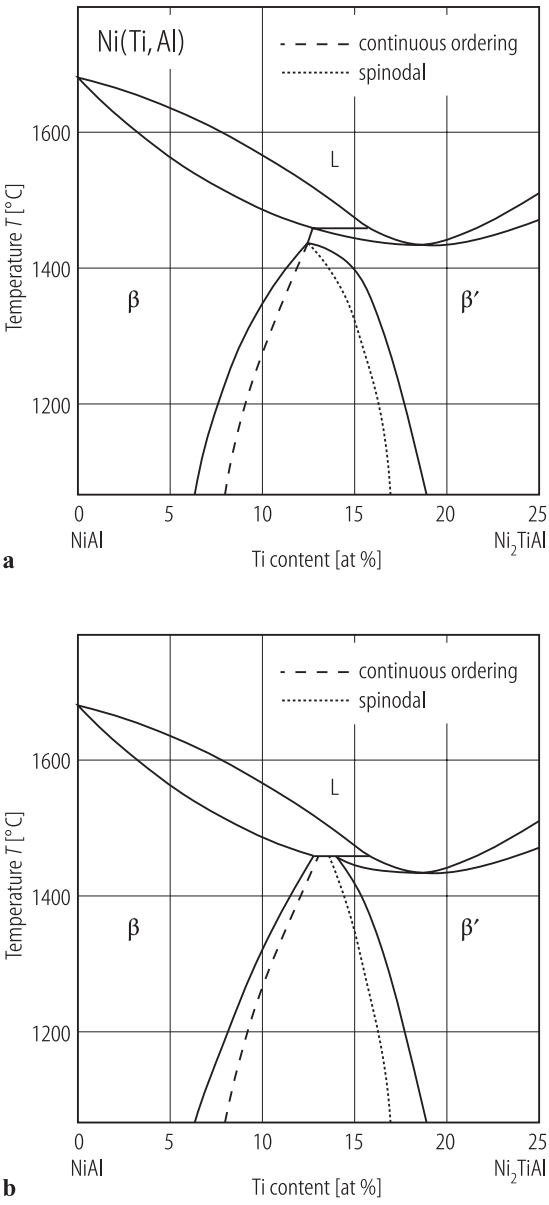

Fig. 42. Two possible phase diagrams for the NiAl/Ni_2TiAl isopleth [89F1].

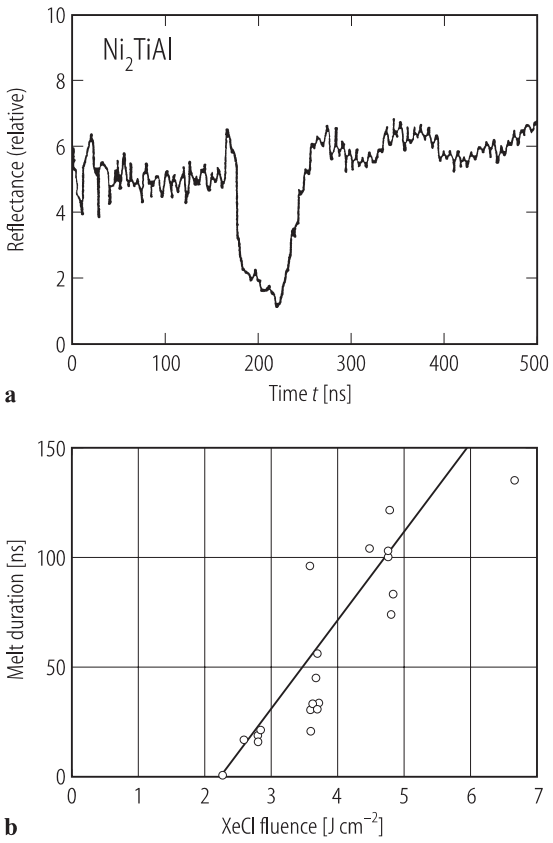

Fig. 44. (**a**) Reflectivity vs. time measured by an Ar^+ ion probe laser from the surface of a Ni_2TiAl sample during surface melting and resolidification with a XeCl laser with a measured fluence of 4.2 J cm^{-2}. (**b**) Measured melt duration vs. fluence data and fit obtained using heat flow model with pulsed laser reflectances of 0.76 and 0.71 for the solid and liquid respectively [91B1].

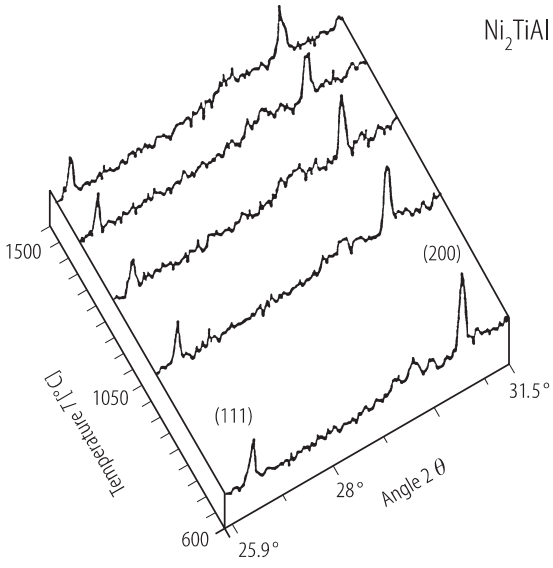

Fig. 43. High temperature X-ray diffraction profiles showing the presence of (111) and (200) peaks at the nominal temperatures of 600, 975, 1350 and 1500 °C indicating the presence of the Heusler $L2_1$ order at all temperatures [91B1].